



**HAL**  
open science

## Non-spherical similarity solutions for dark halo formation

Mark Vogelsberger, Roya Mohayaee, Simon D. M. White

► **To cite this version:**

Mark Vogelsberger, Roya Mohayaee, Simon D. M. White. Non-spherical similarity solutions for dark halo formation. *Monthly Notices of the Royal Astronomical Society*, 2011, 414, pp.3044-3051. 10.1111/j.1365-2966.2011.18605.x . insu-03645947

**HAL Id: insu-03645947**

**<https://insu.hal.science/insu-03645947>**

Submitted on 21 Apr 2022

**HAL** is a multi-disciplinary open access archive for the deposit and dissemination of scientific research documents, whether they are published or not. The documents may come from teaching and research institutions in France or abroad, or from public or private research centers.

L'archive ouverte pluridisciplinaire **HAL**, est destinée au dépôt et à la diffusion de documents scientifiques de niveau recherche, publiés ou non, émanant des établissements d'enseignement et de recherche français ou étrangers, des laboratoires publics ou privés.

# Non-spherical similarity solutions for dark halo formation

Mark Vogelsberger,<sup>1\*</sup> Roya Mohayaee<sup>2</sup> and Simon D. M. White<sup>3</sup>

<sup>1</sup>Harvard–Smithsonian Centre for Astrophysics, 60 Garden Street, MA 02138, USA

<sup>2</sup>Institut d’Astrophysique de Paris (IAP), CNRS, UPMC, 98 bis boulevard Arago, France

<sup>3</sup>Max-Planck Institut für Astrophysik, Karl-Schwarzschild Strasse 1, D-85748 Garching, Germany

Accepted 2011 February 24. Received 2011 February 24; in original form 2010 July 23

## ABSTRACT

We carry out fully three-dimensional simulations of evolution from self-similar, spherically symmetric *linear* perturbations of a cold dark matter (CDM)-dominated Einstein–de Sitter universe. As a result of the radial orbit instability, the haloes which grow from such initial conditions are triaxial with major-to-minor axial ratios of the order of 3:1. They nevertheless grow approximately self-similarly in time. In all cases, they have power-law density profiles and near-constant velocity anisotropy in their inner regions. Both the power-law index and the value of the velocity anisotropy depend on the similarity index of the initial conditions, the former as expected from simple scaling arguments. Halo structure is thus not ‘universal’ but remembers the initial conditions. On larger scales the density and anisotropy profiles show two characteristic scales, corresponding to particles at the first pericentre and at the first apocentre after infall. They are well approximated by the Navarro–Frenk–White model only for one value of the similarity index. In contrast, at all radii within the outer caustic the pseudo-phase-space density can be fitted by a single power law with an index which depends only very weakly on the similarity index of the initial conditions. This behaviour is very similar to that found for haloes formed from  $\Lambda$ CDM initial conditions and so can be considered approximately universal.

**Key words:** dark matter.

## 1 INTRODUCTION

Galaxies are believed to form from gas condensing at the centres of massive dark matter haloes as these grow by collapse and aggregation from weak density fluctuations emerging from the early Universe (White & Rees 1978).

The earliest theoretical insights into the formation and evolution of dark matter haloes were provided by the spherical infall model of Gunn & Gott (1972) and Gott (1975). In this model, an isolated overdensity in an otherwise unperturbed Einstein–de Sitter universe first expands with the Hubble flow, then turns around and collapses. Surrounding material continues to fall on to the object until its mass greatly exceeds that of the originally perturbed region. Asymptotically, a power-law density profile is established with  $\rho \propto r^{-2.25}$ . The late-time structure of this model is a similarity solution whose structure was worked out in detail by Bertschinger (1985). More general similarity solutions where the initial mass perturbation scales with enclosed mass as  $\delta M/M \propto M^{-\epsilon}$  were presented by Fillmore & Goldreich (1984) who showed that these produce haloes with  $\rho \propto r^{-\gamma}$ , where  $\gamma = 2$  for  $0 < \epsilon \leq 2/3$  and  $\gamma = 9\epsilon/(1 + 3\epsilon)$  for  $\epsilon \geq 2/3$ . The change in behaviour at  $\epsilon = 2/3$  reflects the fact that all

orbits are purely radial in these models. No superposition of radial orbits can self-consistently produce a power law shallower than  $r^{-2}$  at small  $r$ . Further generalizations to include randomly oriented rosette orbits with a scale-free eccentricity distribution resulted in spherically symmetric similarity solutions for which  $\gamma = 9\epsilon/(1 + 3\epsilon)$  for all  $\epsilon > 0$  (White & Zaritsky 1992; Sikivie, Tkachev & Wang 1995, 1997; Nusser 2001; MacMillan, Widrow & Henriksen 2006). In such models, the inner density structure of the final haloes reflects the scaling properties of the initial conditions.

In contrast,  $N$ -body simulations have shown for more than a decade that dark matter haloes formed from fully three-dimensional, cosmologically realistic initial conditions do not have pure power-law density profiles. Rather, the logarithmic slope of simulated profiles changes slowly but continuously with radius. In addition, the shape of these profiles is almost independent of halo mass, of cosmological parameters and of the power spectrum of initial fluctuations (Navarro, Frenk & White 1997). The most popular representation of this ‘universal’ shape is the Navarro–Frenk–White (NFW) model which behaves as  $1/r$  in the inner regions and as  $1/r^3$  in the outskirts (Navarro et al. 1997). Even haloes formed by monolithic collapse in the first non-linear phases of hot dark matter (HDM) and warm dark matter models (WDM) are well represented by NFW fits, showing that hierarchical growth is not required to produce this universality (see e.g. Huss, Jain & Steinmetz 1999;

\*E-mail: mvogelsberger@cfa.harvard.edu

Wang & White 2009). Recent  $N$ -body simulations with significantly increased numerical resolution have found small but significant deviations from the NFW shape which depend systematically on halo mass (Hayashi & White 2008; Navarro et al. 2010). Thus, halo density profiles are not truly universal. Nevertheless, these variations are much smaller than those predicted by the similarity solutions, and the profiles can be considered universal to a good approximation.

The differences in behaviour between similarity solutions and numerical simulations reflect the fact that the former enforce spherical symmetry and a potential which varies smoothly with time according to the similarity scaling, while the latter involve strongly time-dependent and fully three-dimensional potential fluctuations which exchange energy and angular momentum between different parts of the system through the classical ‘violent relaxation’ mechanism (Lynden-Bell 1967). Even though extensions of the original similarity solutions allow non-radial orbits with a variety of eccentricity distributions (White & Zaritsky 1992; Sikivie et al. 1995, 1997; Nusser 2001; MacMillan et al. 2006), they retain both spherical symmetry and strict similarity scaling, and so exclude violent relaxation and any possibility for it to drive convergence towards a universal (i.e.  $\epsilon$ -independent) non-linear structure. Large and time-dependent potential fluctuations are required to produce such convergence. These occur naturally not only in hierarchical assembly models but also in other situations, for example during the monolithic, quasi-ellipsoidal collapse of the first generation of haloes in HDM or WDM cosmologies (Zel’Dovich 1970; Sheth, Mo & Tormen 2001; Wang & White 2009).

It has long been known that spherical equilibria dominated by radial orbits are violently unstable and evolve on a few dynamical times into strongly ellipsoidal bars with significant non-radial motions (Antonov 1973; Henon 1973; Polyachenko 1981; Polyachenko & Shukhman 1981; Barnes 1985; Merritt & Aguilar 1985; Meza & Zamorano 1997). The original similarity solutions of Fillmore & Goldreich (1984) and Bertschinger (1985) are thus not viable models for the formation of real systems – the slightest non-spherical perturbation of their quasi-equilibrium inner regions causes rapid evolution to an entirely different non-linear structure. A number of authors have noted situations where the radial orbit instability gives rise to haloes with NFW-like density profiles (Henriksen & Widrow 1999; Huss et al. 1999; Barnes et al. 2005; MacMillan et al. 2006; Bellovary et al. 2008). There are thus (at least) two possibilities for the long-term evolution of structure from (almost) spherically symmetric, self-similar linear initial conditions. Either it may approach a non-spherical self-similar solution, which would then have a potential which changes smoothly in time and no violent relaxation, or the strongly time-dependent behaviour may continue indefinitely, allowing violent relaxation to rearrange material in the inner regions. In the former case an NFW-like universal profile is only consistent with similarity scaling for  $\epsilon = 1/6$ , whereas in the latter case an NFW-like profile could, in principle, be maintained at all times.

In this paper, we investigate these issues by simulating evolution from spherically symmetric, self-similar, linear initial conditions for a variety of values of  $\epsilon$ . As we showed in Vogelsberger et al. (2009), particle noise leads to the rapid onset of the radial orbit instability in such simulations, so that their later non-linear evolution is strongly non-spherical. Here we show that while some chaotic time dependence remains at late times, evolution is nevertheless approximately self-similar. The inner structure of the haloes remembers the initial conditions from which they formed, depending on  $\epsilon$  in the same way as in the spherical similarity solutions.

In Section 2, we present our simulations and study the formation of ellipsoidal ‘bars’. In Section 3, we study how these bars affect the velocity anisotropy and density profiles in the inner halo. The transition between the infall and quasi-equilibrium regions, and the inner and outer scales which define it is discussed in Section 4. Finally in Section 5 we demonstrate that, in contrast to the velocity anisotropy and density profiles, the profile of pseudo-phase-space density is almost universal in these models.

## 2 RADIAL ORBIT INSTABILITY: BAR FORMATION

The similarity solutions assume an Einstein–de Sitter universe in which the linear mass perturbation  $\delta M_i$  within a sphere containing unperturbed mass  $M_i$  initially satisfies

$$\frac{\delta M_i}{M_i} = 1.0624 \left( \frac{M_i}{M_0} \right)^{-\epsilon}, \quad (1)$$

where  $\epsilon$  is a scaling index and  $M_0$  is a reference mass taken to be the mass within the turnaround radius ( $r_{\text{ta}}$ ) at the initial time. The parameter  $\epsilon$  is restricted to positive values in order to ensure that more distant mass shells turn around and fall back later than inner ones. The mass within the shell that is just turning around and the physical radius of this shell at turnaround then scale with time as  $M_{\text{ta}} \propto t^{2/3\epsilon}$  and  $r_{\text{ta}} \propto t^{2/3+2/9\epsilon}$  so that the mean mass density contained within the turnaround radius is always 5.5 times the cosmic mean (the critical density) and so satisfies  $\rho_{\text{ta}} \propto t^{-2}$ .

Since these initial conditions are spherically symmetric, the system remains spherically symmetric at later times (if instabilities are ignored/suppressed) and the particles on each spherical shell all execute identical though differently oriented radial orbits. The scale-free nature of the initial conditions ensures that the orbits executed by different shells are identical when scaled to their individual turnaround radii and times. Gunn & Gott (1972) showed that at radii much smaller than  $r_{\text{ta}}$  this results in a stable halo with density profile  $\rho \propto r^{-9/4}$  when  $\epsilon = 1$ , the only case they considered. Fillmore & Goldreich (1984) generalized this to other values of  $\epsilon$ , finding the inner profile to vary with the initial scaling properties:

$$\rho(r) \propto \begin{cases} r^{-2}, & \epsilon \leq \frac{2}{3} \\ r^{-9\epsilon/(1+3\epsilon)}, & \epsilon \geq \frac{2}{3}. \end{cases} \quad (2)$$

The change of behaviour at  $\epsilon = 2/3$  is due to the fact that no self-consistent spherical equilibrium system built from radial orbits can have a power-law slope shallower than  $-2$ , because every particle is constrained to pass through the centre of the system once per orbit. The full structure of the similarity solution for the case  $\epsilon = 1$  was worked out by Bertschinger (1985), who showed that the power-law inner structure breaks in the transition to the infall regime and that the confinement of non-zero phase-space density to a three-dimensional sheet results in a series of sharp spherical caustics which are superposed on the inner power-law density profile and are located at any given time at the positions of particles currently passing through apocentre.

In this paper, we simulate evolution from initial conditions which obey the spherical similarity solutions, exactly as in Vogelsberger et al. (2009), but for a variety of values of  $\epsilon$ . We use a fully three-dimensional  $N$ -body solver, a version of GADGET-2 (Springel 2005), and we allow particle noise to drive the radial orbit instability. This happens in the first few expansion factors so that the later stages of the simulations all contain fully developed ellipsoidal ‘bars’. All our simulations follow evolution over a factor of 1000 in time

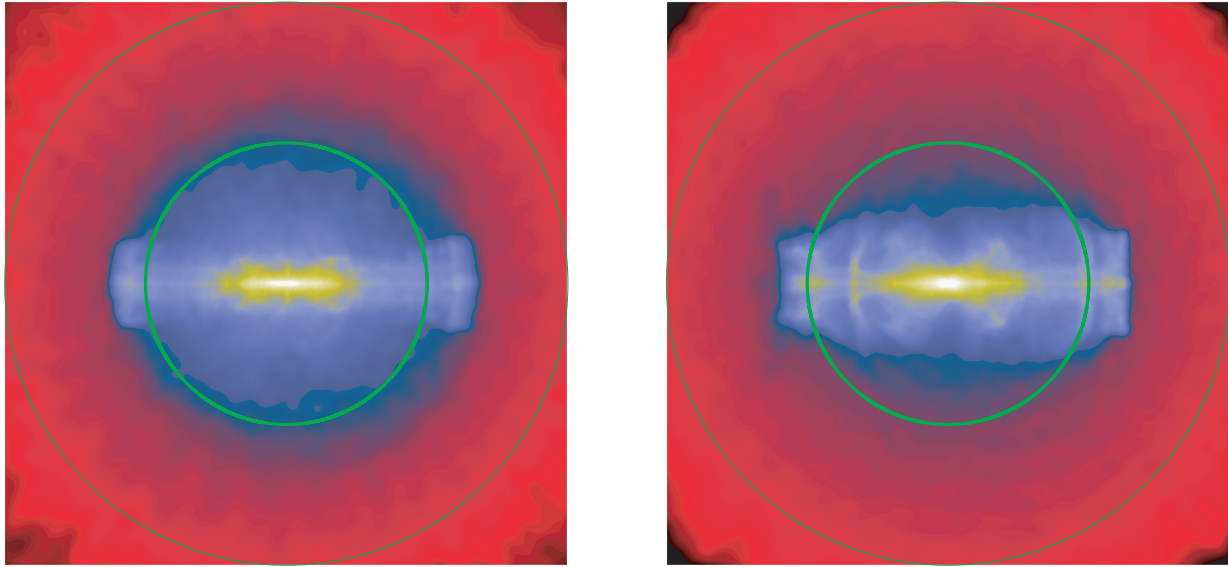


**Figure 1.** Projected density maps of the haloes formed for  $\epsilon = 0.4$  (left-hand panel) and  $\epsilon = 0.8$  (right-hand panel). In each case, the long axis of the bar is horizontal, its short axis is vertical and the region plotted is a slice of thickness  $2r_{\text{outer caustic}}$  and side  $4r_{\text{outer caustic}}$  where  $r_{\text{outer caustic}}$  is the radius of the outer caustic (first apocentre after the turnaround) in the spherical similarity solution. The thick and thin green circles have radii of  $r_{\text{outer caustic}}$  and  $2r_{\text{outer caustic}}$ , respectively. In units of the outer-caustic radius, the bar length is approximately ‘universal’, although time-dependent features are still visible in these plots, for example in the lack of left–right symmetry.

corresponding to expansion of the background cosmology from  $a = 0.01$  and until  $a = 1$ . The softening length is kept fixed in comoving coordinates at  $0.00025r_{\text{ta}}(a = 1)$ . The final halo is represented by about  $256^3/2 \sim 8.4 \times 10^6$  particles within  $r_{\text{ta}}$ .

In Fig. 1 we show images of the bar in the final state of two of our simulations,  $\epsilon = 0.4$  on the left and  $\epsilon = 0.8$  on the right. In each case the bars extend slightly beyond the position of the outer caustic of the corresponding spherical similarity solution, which we indicate with a green circle. The location of the actual outer caustic corresponds to the transition in colour from blue to red. In all our simulations, we find bars with semimajor axes (delineated by the outer caustics) which are about 1.2 times the radius of the spherical caustic. Thus measured in units of the latter, our bar lengths appear universal. In both the cases shown, there are clear left–right asymmetries in the inner structure of the bars (the yellow regions). Such asymmetry is a clear indicator of the time-dependent behaviour – any exact non-spherical similarity solution is expected to be left–right symmetric.

We show the axial ratios of equidensity surfaces of our final bars as a function of the semimajor axis in the left-hand panel of Fig. 2. These ratios were obtained by calculating the moment of inertia of all particles within an ellipsoidal surface, deriving the eigenvalues and principal axes, and then iterating until the shape and orientation of the bounding ellipsoid are consistent with the orientation and relative axis lengths inferred from the moment of inertia. These ratios are thus cumulative, referring to all material interior to the quoted radius rather than an ellipsoidal shell at this radius. The axial ratios take their most extreme values just inside the outer caustic, with all simulations giving minor-to-major values close to 0.2 and intermediate-to-major values close to 0.35. They approach unity rapidly at larger radii and also rise steadily though more slowly towards smaller radii. There is no clear trend as a function of  $\epsilon$ , suggesting that the exact values may be stochastically determined and perhaps also time-dependent. We test this in the right-hand panel by replotting the curves using a thick linestyle and comparing them with results at  $a = 0.5$ , represented by thin lines. The overall pattern

is very similar at the two times. There is some indication that the deviation of individual models from the mean is coherent between the two times, but there are also substantial variations. Time-dependent effects appear to be influencing the measurements significantly, and these plausibly have a relatively long time coherence. In consequence, it is not possible to decide whether the apparent trends with  $\epsilon$  are real or just reflect unrelated time-dependent variations. The overall similarity of all the curves at both times suggests that the shape behaviour is approximately both self-similar and ‘universal’.

### 3 DENSITY AND VELOCITY ANISOTROPY PROFILES

The central bar torques infalling particles, inducing non-radial motions which transform the purely radial orbits of the original similarity solution into fully three-dimensional orbits. This alters both the density and the velocity dispersion structure of the non-linear regions, as we now illustrate. A velocity anisotropy parameter is conventionally defined as

$$\beta(r) = 1 - \sigma_t^2/\sigma_r^2, \quad (3)$$

where  $\sigma_r(r)$  and  $\sigma_t(r)$  are one-dimensional radial and transverse velocity dispersions, respectively, averaged over spherical shells of radius  $r$ . The left-hand panel of Fig. 3 shows  $\beta(r)$  at two different times,  $a = 0.5$  (dashed lines) and  $a = 1$  (solid lines). The right-hand panel shows  $(r/r_{\text{ta}})^2 \rho(r)/\rho_b$  at the same two times. The two quantities are evaluated using the same set of logarithmically spaced spherical shells. Neither profile changes systematically with time when plotted against  $r/r_{\text{ta}}$ , consistent with the expectations of self-similar evolution.

The spherically averaged density profiles in the right-hand panel of Fig. 3 show three distinct regimes. At radii larger than the outer caustic, only one (infalling) matter stream is present. Here, there is essentially perfect agreement between  $a = 0.5$  and 1 in all cases, and the effective power-law index of the profile is significantly

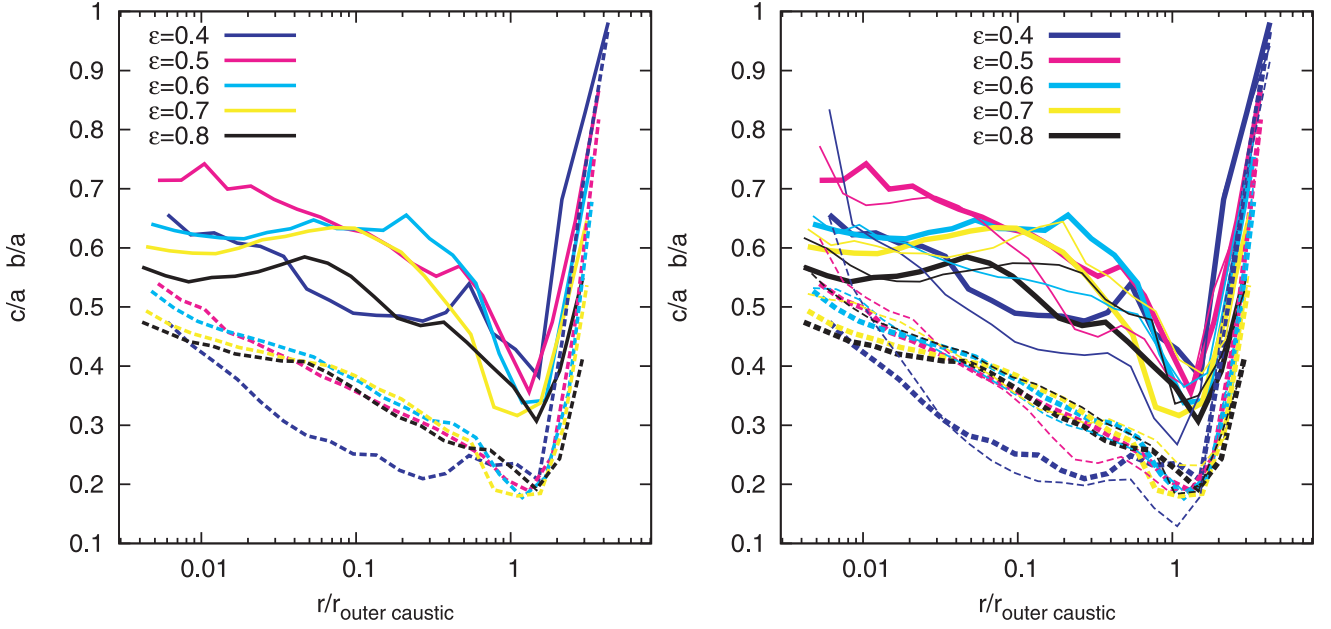


**Figure 2.** Left-hand panel: halo axial ratios as a function of radius for a variety of similarity scaling parameters. Different colours correspond to different values of the scaling parameter  $\epsilon$ . For each  $r$ , axial ratios are estimated from the principal values of an inertia tensor calculated for all particles within an ellipsoid of mean radius  $r$ . Dashed lines denote minor-to-major axial ratios while solid lines denote intermediate-to-major ratios. For each simulation, radii are normalized by that of the outer caustic in the corresponding similarity solution. This panel shows results for the final time  $a = 1$ . Right-hand panel: axial ratios replotted as thick lines and compared with results for  $a = 0.5$  (thin lines).

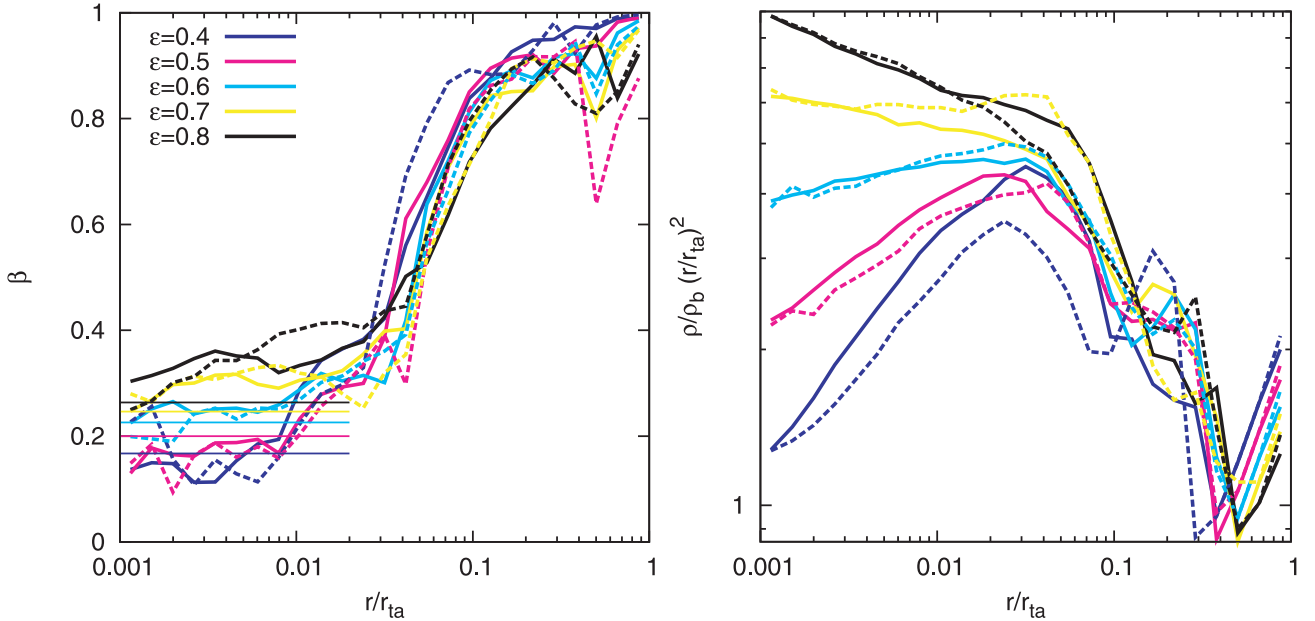


**Figure 3.** Left-hand panel: velocity anisotropy  $\beta(r) = 1 - \sigma_t^2 / \sigma_r^2$  as a function of radius  $r$ , normalized by the turnaround radius  $r_{ta}(t)$ . Here  $\sigma_r(r)$  and  $\sigma_t(r)$  are the one-dimensional radial and transverse velocity dispersions averaged over spherical shells, respectively. Different colours denote simulations with different values of  $\epsilon$  as indicated. Solid lines are for  $a = 1$  and dashed lines for  $a = 0.5$ . Beyond the outer caustic, all particles are falling in for the first time, but they nevertheless have non-zero radial and tangential velocity dispersions because the quadrupole moment of the ellipsoidal inner regions induces variations in infall velocity and infall direction at each  $r$ . Both dispersions jump dramatically as the outer caustic is crossed and the anisotropy is slowly varying and relatively small in the inner quasi-equilibrium regions. The softening radius is too small to affect the velocity dispersions over the radial range plotted. Thin horizontal lines show the asymptotic values of equation (5). Right-hand panel: mass density averaged in spherical shells as a function of radius, again normalized by  $r_{ta}$ . Line colours and types correspond to those in the left-hand panel. The density is given in units of the current critical density and is multiplied by  $(r/r_{ta})^2$  to suppress the dominant dependence and to allow easier comparison of the curves. In both panels, the structure is very similar at the two times considered. The dependence on  $\epsilon$  is very clear in the density profiles and also appears significant in the anisotropy profiles.

greater than  $-2$  and similar for all  $\epsilon$ . Only the position of the outer caustic (in units of  $r_{\text{ta}}$ ) varies significantly with  $\epsilon$ . Between this outer caustic and the typical radii of particles passing their first pericentre after turnaround,<sup>1</sup> the density profile has a mean effective index which is similar for all  $\epsilon$  and substantially less than  $-2$ . The behaviour in this regime is quite irregular, however, and there are substantial differences between  $a = 0.5$  and  $1$  in several cases. Examination of phase-space plots (see e.g. fig. 8 of Vogelsberger et al. 2009) suggests that this time dependence is driven by large-scale irregularities which grow around the first apocentre after turnaround but are washed out by phase-mixing at later times. Inside the radius of the first pericentre, the profiles become more regular and agree well between the two times shown. To a good approximation, they are power laws that are well fitted (as  $r \rightarrow 0$ ) by

$$\rho(r) \propto r^{-9\epsilon/(1+3\epsilon)}, \quad \epsilon > 0. \quad (4)$$

This is the value expected for a perfect similarity solution in the presence of non-radial motions (White & Zaritsky 1992; Sikivie et al. 1995, 1997; Nusser 2001; MacMillan et al. 2006), demonstrating that the time-dependent behaviour seen at intermediate radii is not sufficient to destroy the similarity scaling and enforce ‘universal’ structure. Note that both the steep slope over the decade immediately inside the outer-caustic radius (which is roughly at the conventional virial radius) and the break to a shallower slope at smaller radii are qualitatively similar to the ‘universal’ behaviour encapsulated by the NFW profile. However, the inner slope matches the NFW value only for  $\epsilon = 1/6$ , smaller than any of the values tested here.

The left-hand panel of Fig. 3 shows that velocity anisotropy profiles are similar for all values of  $\epsilon$ , exhibiting distinct behaviour in the same three regimes seen in the density profiles. At large radii, particles are falling in for the first time on very nearly radial orbits, gradually gaining angular momentum as they feel the quadrupole moment of the central bar. As they cross the outer caustic they are mixed with particles which have already passed pericentre, and  $\beta(r)$  drops to much smaller values. Inside the radius of the first pericentre,  $\beta(r)$  is almost constant in the quasi-equilibrium region, declining slightly towards the centre. In this region there appears to be a weak but significant dependence of anisotropy on the similarity index, with larger values of  $\epsilon$  giving rise to slightly more radially biased velocity dispersions. This behaviour is a consequence of the dependence of the inner density profile on  $\epsilon$ . For larger  $\epsilon$ , the inner mass distribution is more strongly centrally concentrated, so that its quadrupole moment becomes less significant relative to the monopole and less angular momentum is induced in the orbits of infalling particles.

The left-hand panel of Fig. 3 suggests that in the inner part of the halo, the  $\beta$  parameter may approach an asymptotic value which depends on the value of  $\epsilon$ . Hansen & Moore (2006) have proposed that the equation  $\beta(r) = -0.2(d \ln \rho / d \ln r + 0.8)$  relates velocity anisotropy and density profile slope in the inner parts of dark matter haloes (see also e.g. Navarro et al. 2010). Using equation (4) which is indeed valid in the inner part of our haloes, the above relationship reduces to

$$\beta = 0.2 \left[ \frac{9\epsilon}{(1+3\epsilon)} - 0.8 \right], \quad \epsilon > 0, \quad (5)$$

which gives  $\beta = \{0.17, 0.2, 0.23, 0.25, 0.26\}$  for  $\epsilon = \{0.4, 0.5, 0.6, 0.7, 0.8\}$ . These values are in reasonable agreement with those

inferred from the left-hand panel of Fig. 3, even though our haloes form in a quite different (and ‘non-universal’) manner from cold dark matter (CDM) haloes.

#### 4 INNER AND OUTER SCALES: FIRST PERICENTRE AND OUTER-CAUSTIC RADII

In the previous section, we found approximate similarity behaviour for non-spherical haloes formed by infall from power law and almost spherically symmetric initial conditions. As in the fully spherically symmetric similarity solution of Bertschinger (1985), the resulting non-linear density profile is a power law only at sufficiently small radii, but in our case the transition between the infall and quasi-equilibrium regimes is more complex than when the orbits are purely radial. As we have seen, there appear to be two distinct scales: an inner scale at around  $0.01r_{\text{ta}}$  and an outer scale at around  $0.1r_{\text{ta}}$ . In the last section, we asserted that the former can be associated with the first pericentric passage of infalling particles and the latter with the following apocentric passage, which occurs at the outer caustic. Here we support these assertions by a more careful study of the radial position of these orbital turning points.

In the spherical similarity solution, the outer caustic is the border between the one- and three-stream regions. Outside this radius all particles are falling in for the first time, while within it many of them have passed through the centre at least once. In Fig. 4, we show how the radius of this outer caustic, evaluated directly from the similarity solution, increases with  $\epsilon$ . Comparison with the right-hand panel of Fig. 3 shows that the sharp change in profile shape which delineates the inner boundary of the infall regime in our simulations is indeed very close to this radius and depends on  $\epsilon$  exactly as predicted.

In Fig. 3, all radii are expressed in units of the turnaround radius. Although this is the natural scale for models with spherically symmetric initial perturbations of the kind studied here, it turns out that scaling to the outer-caustic radius (i.e. the position of the first apocentre after turnaround) results in greater uniformity of the inner non-linear structure of our haloes as a function of  $\epsilon$ . We show this in Fig. 5 which may be compared with Fig. 3. Note that in the

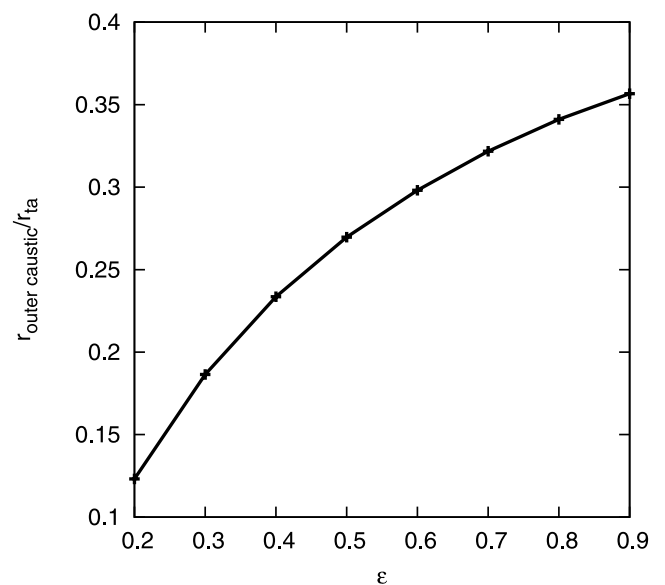


**Figure 4.** The radius of the first apocentre after turnaround (i.e. the outer-caustic radius) in units of the current turnaround radius as a function of  $\epsilon$  in the spherically symmetric similarity solutions with radial orbits.

<sup>1</sup> We investigate these scales in more detail below.

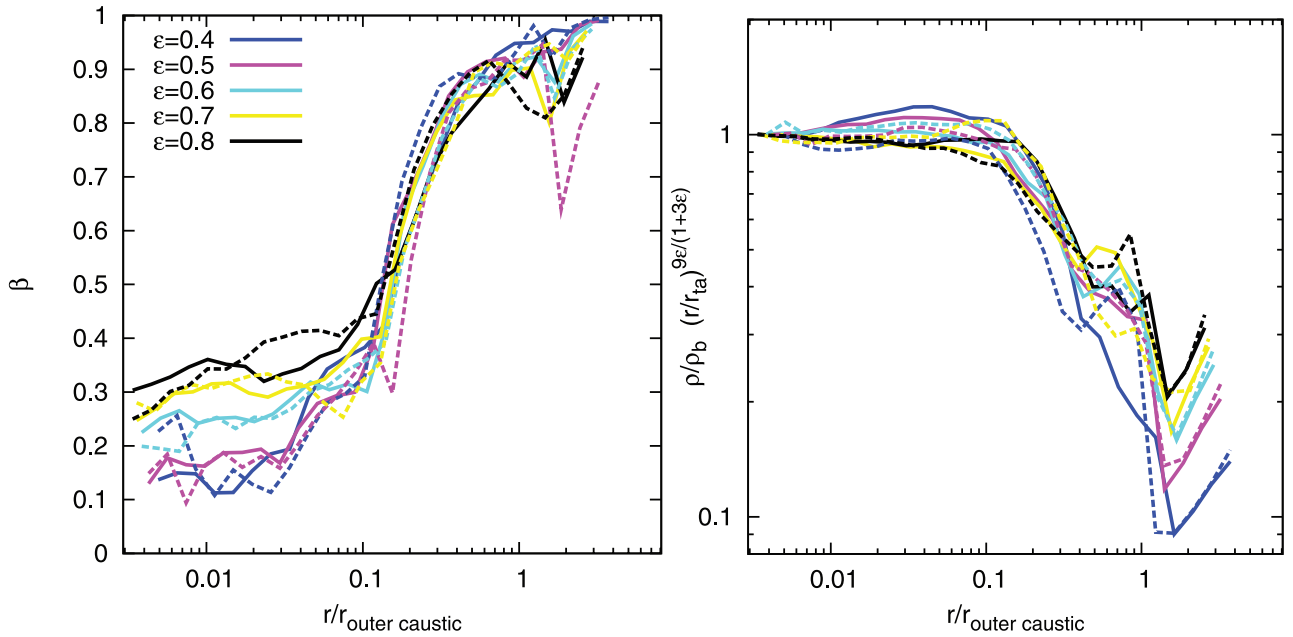


**Figure 5.** Using the radius of the outer caustic as a characteristic scale makes the non-linear structure of haloes appear almost independent of  $\epsilon$ . The left-hand and right-hand panels show the effect of using this scaling on the velocity anisotropy and density profiles, respectively. In the right-hand panel, the y-axis is furthermore multiplied by an  $\epsilon$ -dependent power law of radius chosen so that the inner profile appears flat and equal to unity (see equation 4). Solid lines show the  $a = 1$  profiles, whereas dashed lines show the profiles at time  $a = 0.5$ .

right-hand panel of Fig. 5, the outer transition occurs slightly beyond the nominal outer-caustic radius. This is because we have rescaled using the value for the spherically symmetric similarity solution, as plotted in Fig. 4. This is slightly smaller than the caustic radius at the end of our numerical bars, as is clearly visible in Fig. 1.

Next, we consider the inner scale at around  $0.01 r_{ta}$  (see Fig. 3). We follow the trajectories of all simulation particles and record the radial position of their first pericentric passage. For all particles which pass the first pericentre between  $a = 0.5$  and 1, we follow their radial position  $r$  along their orbit and record its first minimum as well as the time when this minimum occurs. The latter allows us to calculate the position of the outer caustic (according to the spherical similarity solution) at the time of pericentric passage and thus to measure the ratio of these two lengths. A histogram of  $r_{peri}/r_{outer\ caustic}$  is presented in Fig. 6. There is considerable scatter in this ratio because pericentric radius depends strongly on the angle between the infall direction of a particle and the long axis of the bar. It is very small for infall along one of the principal axes, and it maximizes at angles well away from any of these axes. Nevertheless, there is a well-defined ‘typical’ pericentric distance which is  $\sim 0.1 r_{outer\ caustic}$  for all values of  $\epsilon$ . This agrees well with the inner transition scale of the  $\beta$  and density profiles in Figs 3 and 5.

## 5 PSEUDO-PHASE-SPACE DENSITY PROFILES

A property of dark matter haloes with rather intriguing characteristics is the pseudo-phase-space density. This is defined as  $\rho/\sigma^3$ , where  $\rho(r)$  and  $\sigma(r)$  are the mass density and the (three-dimensional) velocity dispersion averaged over a shell of radius  $r$ , respectively. Even though neither  $\rho(r)$  nor  $\sigma(r)$  is itself close to a power law, this particular combination is very close to a power law for haloes formed from  $\Lambda$ CDM initial conditions, and, remarkably, its power-law index is very similar to that found in the spherically

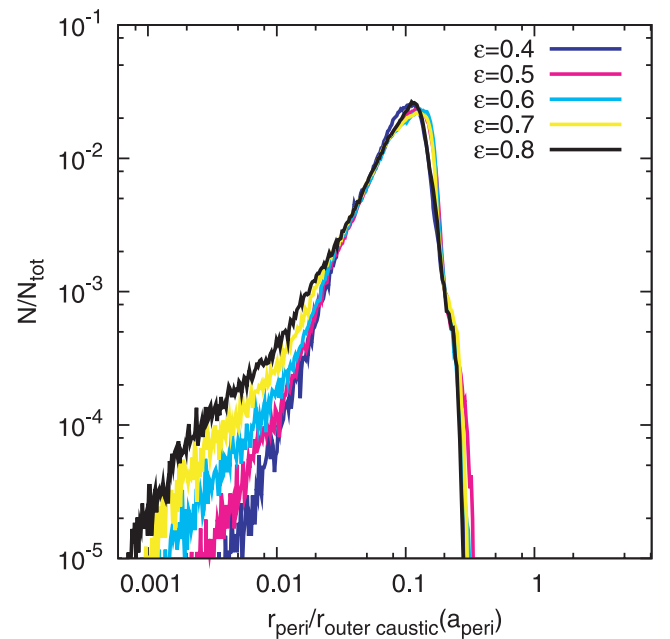


**Figure 6.** Histograms of the first pericentre distance, measured directly from our simulations, in units of the fiducial current outer-caustic radius given in Fig. 4. In these units, the distribution of the first pericentre distance is almost independent of  $\epsilon$ , peaking at about 0.1.

symmetric similarity solution of Bertschinger (1985). This curiosity was first pointed out by Taylor & Navarro (2001), and since that time it has been investigated by many authors who have found the behaviour to be quite robust, to extend over more than three decades in radius and to hold also for other kinds of initial conditions (see e.g. Ludlow et al. 2010; Navarro et al. 2010).

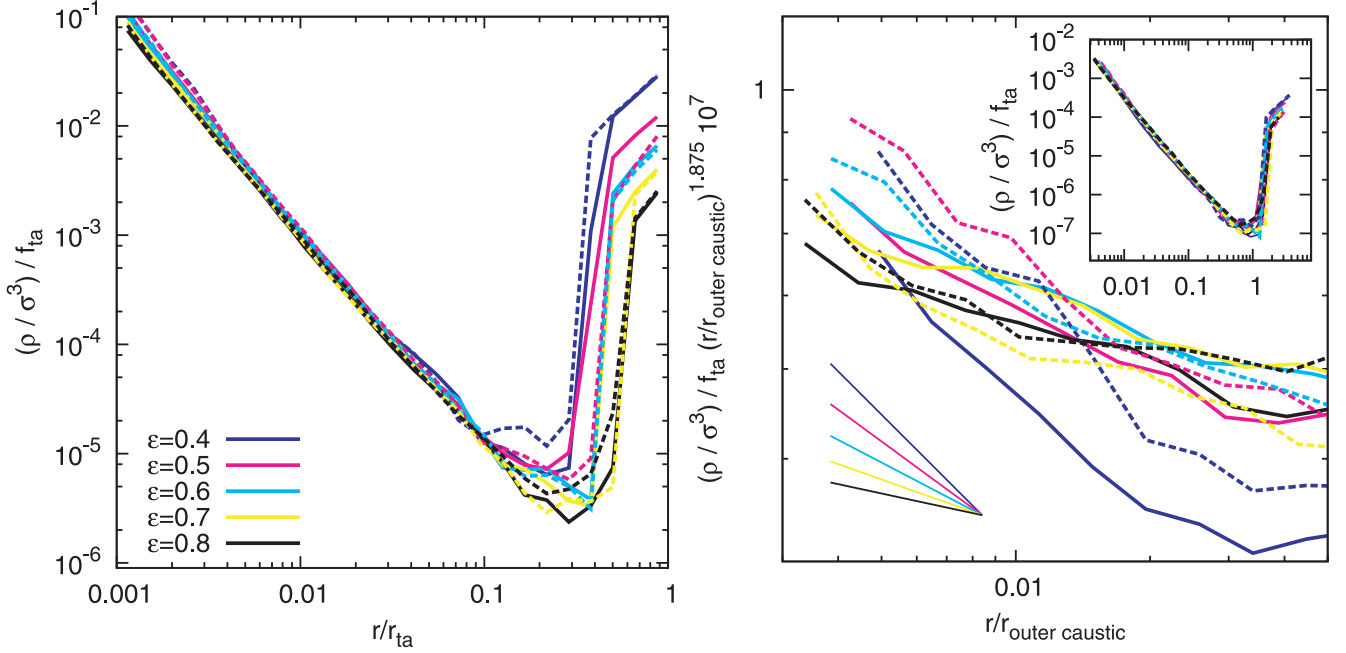


**Figure 7.** Left-hand panel: pseudo-phase-space density profiles for various  $\epsilon$  evaluated at  $a = 0.5$  (dashed) and  $a = 1$  (solid). The radial coordinate is scaled with  $r_{\text{ta}}$  and the pseudo-phase-space density with  $f_{\text{ta}} \equiv \rho_b t^3 / r_{\text{ta}}^3$ . With these scalings, the profiles do not change significantly with time and, remarkably, are very similar and are close to a power law within the outer caustic for all  $\epsilon$ , even though they differ in the infall region. There is no obvious feature at the radius of the first pericentre. Right-hand panel: pseudo-phase-space density profiles of the inner parts of our haloes after rescaling the horizontal and vertical axes by  $r_{\text{ta}}/r_{\text{outer caustic}}$  and  $(r_{\text{outer caustic}}/r_{\text{ta}})^3$ , respectively. This scaling brings the overall profiles into quite close agreement within the outer caustic, as can be seen in the inset. The slope of the inner profile nevertheless depends weakly on  $\epsilon$ . In the main panel, we have additionally scaled by  $r^{1.875}$  the inverse of the behaviour expected theoretically for  $\epsilon = 1$ . Dashed lines show the pseudo-phase-space density profiles at  $a = 0.5$ . The thin straight lines in the lower left indicate the slopes of the analytic predictions of equation (6).

In the framework of a true similarity solution with non-radial motions, the inner density profile must obey equation (4) for all  $\epsilon > 0$  and  $\beta(r)$  must become constant at small radii. Since the circular velocity and the velocity dispersions must have the same scaling behaviour, the pseudo-phase-space density is also a power law which is easily verified to be

$$\frac{\rho}{\sigma^3} \propto r^{-3(2+3\epsilon)/(2(1+3\epsilon))} \quad \text{for all } \epsilon. \quad (6)$$

For the original similarity solutions of Fillmore & Goldreich (1984) which had purely radial orbits, this behaviour holds only for  $\epsilon \geq 2/3$ . The specific case  $\epsilon = 1$  studied by Bertschinger (1985) gives  $\rho/\sigma^3 \propto r^{-15/8}$ .

We have directly evaluated the pseudo-phase-space density profiles of our simulated haloes using logarithmic bins in radius and subtracting the mean radial motion before evaluating the velocity dispersion. We show the results in Fig. 7. In the left-hand panel, the radial coordinate is normalized by the turnaround radius and the pseudo-phase-space density by the characteristic value  $f_{\text{ta}} \equiv \rho_b t^3 / r_{\text{ta}}^3$ . The very good agreement between the curves for  $a = 0.5$  and 1 demonstrates that the pseudo-phase-space density evolves self-similarly in time. This is no surprise, given that we have already seen good scaling for the density and velocity anisotropy profiles. More surprising is the fact that inside the outer-caustic radius, the profiles show very little dependence on  $\epsilon$ , either in slope or in amplitude. Furthermore, they are all good approximations to a power law, and there is no obvious feature near the radius of the first pericentre despite the very strong features seen at this radius in Fig. 3. Once again scaling to the radius of the outer caustic gives an even better overlap since it matches the break at large radii, as can be seen in the inset in the right-hand panel.

We focus on the innermost part of our haloes (the regions inside the first pericentre) in the main plot of the right-hand panel of Fig. 7. We again use the outer-caustic radius to scale the radii and pseudo-phase-space densities, and we additionally multiply the pseudo-phase-space density by  $r^{15/8}$  to take out the dominant trend. The power-law slopes expected for exact similarity scaling are indicated by thin straight lines and are seen to be a good but not perfect fit to the simulated behaviour. The differences are small enough that they can probably be ascribed to residual time-dependent behaviour, an interpretation which is supported by the differences between the  $a = 0.5$  and 1 curves for each  $\epsilon$ .

Thus, unlike the velocity anisotropy and the density profiles, the pseudo-phase-space density profile is close to a power law over the full non-linear extent of our haloes and it depends only very weakly on  $\epsilon$ . Thus, to a good approximation it can be considered ‘universal’.

## 6 CONCLUSIONS

We have shown that although the classic spherically symmetric similarity solutions of Fillmore & Goldreich (1984) and Bertschinger (1985) are violently unstable to the radial orbit instability, evolution from the initial conditions they presuppose gives rise to ellipsoidal, bar-like haloes which nevertheless grow in an approximately self-similar way.

The non-linear structure of these objects shows two characteristic radii. The outer caustic separates the infall and multistream regions and occurs at approximately the same position as in the original spherically symmetric similarity solutions. The second characteristic radius is about an order of magnitude smaller and occurs at the

typical first pericentre distance of the infalling particle stream. It can be considered the outer edge of the quasi-equilibrium region. Relative to the turnaround radius, both radii increase with the value of the similarity parameter  $\epsilon$ .

Both the density and velocity anisotropy profiles show strong features at the first pericentre radius. Within this radius, the density profile is approximately a power law,  $\rho \propto r^{-\gamma}$  with  $\gamma = 9\epsilon/(1 + 3\epsilon)$ , and the velocity anisotropy is approximately constant,  $\beta = 0.2(\gamma - 0.8)$ . At larger radii, the density profile becomes substantially steeper and the velocity anisotropy rises steeply.

Despite the strong features in the density and velocity anisotropy profiles at the first pericentre radius, the pseudo-phase-space density profiles of all our haloes are close to power laws all the way out to the outer-caustic radius. Furthermore, they depend only very weakly on  $\epsilon$  and are similar to the profiles of haloes formed from  $\Lambda$ CDM initial conditions. Thus, this profile seems remarkably ‘universal’.

## ACKNOWLEDGMENTS

Our simulations were carried out at the Computing Centre of the Max-Planck-Society in Garching. RM thanks French ANR OTARIE for support. We thank Niayesh Afshordi, Ed Bertschinger, James Binney, Jacques Colin, Aaron Ludlow and Julio Navarro for useful discussions.

## REFERENCES

Antonov V. A., 1973, in Omarov T. B., ed., *Dynamics of Galaxies and Star Clusters*. Nauka, Alma Ata, p. 139  
 Barnes J., 1985, in Goodman J., Hut P., eds, *Proc. IAU Symp. 113, Dynamics of Star Clusters*. Reidel, Dordrecht, p. 297  
 Barnes E. I., Williams L. L. R., Babul A., Dalcanton J. J., 2005, *ApJ*, 634, 775

Bellovary J. M., Dalcanton J. J., Babul A., Quinn T. R., Maas R. W., Austin C. G., Williams L. L. R., Barnes E. I., 2008, *ApJ*, 685, 739  
 Bertschinger E., 1985, *ApJS*, 58, 39  
 Fillmore J. A., Goldreich P., 1984, *ApJ*, 281, 1  
 Gunn J. E., Gott J. R. I., 1972, *ApJ*, 176, 1  
 Gott J. R. I., 1975, *ApJ*, 201, 296  
 Hansen S. H., Moore B., 2006, *New Astron.*, 11, 333  
 Hayashi E., White S. D. M., 2008, *MNRAS*, 388, 2  
 Hénon M., 1973, *A&A*, 24, 229  
 Henriksen R. N., Widrow L. M., 1999, *MNRAS*, 302, 321  
 Huss A., Jain B., Steinmetz M., 1999, *ApJ*, 517, 64  
 Ludlow A. D., Navarro J. F., Springel V., Vogelsberger M., Wang J., White S. D. M., Jenkins A., Frenk C. S., 2010, *MNRAS*, 718  
 Lynden-Bell D., 1967, *MNRAS*, 136, 101  
 MacMillan J. D., Widrow L. M., Henriksen R. N., 2006, *ApJ*, 653, 43  
 Merritt D., Aguilar L. A., 1985, *MNRAS*, 217, 787  
 Meza A., Zamorano N., 1997, *ApJ*, 490, 136  
 Navarro J. F., Frenk C. S., White S. D. M., 1997, *ApJ*, 490, 493  
 Navarro J. F. et al., 2010, *MNRAS*, 402, 21  
 Nusser A., 2001, *MNRAS*, 325, 1397  
 Polyachenko V. L., 1981, *Soviet Astron. Lett.*, 7, 79  
 Polyachenko V. L., Shukhman I. G., 1981, *Astron. Zh.*, 58, 933  
 Sheth R. K., Mo H. J., Tormen G., 2001, *MNRAS*, 323, 1  
 Sikivie P., Tkachev I. I., Wang Y., 1995, *Phys. Rev. Lett.*, 75, 2911  
 Sikivie P., Tkachev I. I., Wang Y., 1997, *Phys. Rev. D*, 56, 1863  
 Springel V., 2005, *MNRAS*, 364, 1105  
 Taylor J. E., Navarro J. F., 2001, *ApJ*, 563, 483  
 Vogelsberger M., White S. D. M., Mohayaee R., Springel V., 2009, *MNRAS*, 400, 2174  
 Wang J., White S. D. M., 2009, *MNRAS*, 396, 709  
 White S. D. M., Rees M. J., 1978, *MNRAS*, 183, 341  
 White S. D. M., Zaritsky D., 1992, *ApJ*, 394, 1  
 Zel'Dovich Y. B., 1970, *A&A*, 5, 84

This paper has been typeset from a  $\text{\TeX}/\text{\LaTeX}$  file prepared by the author.